A Dynamically-Consistent Ocean Climatology and Its Temporal Variations

Ichiro Fukumori[*], Patrick Heimbach [†], Rui M. Ponte[‡] and Carl Wunsch[§] [¶]

[*]Jet Propulsion Laboratory, Pasadena, CA

[†]University of Texas at Austin, Austin Texas

[‡]Atmospheric and Environmental Research, Inc., Lexington, Massachusetts

[§]*Corresponding author address:* Carl Wunsch

E-mail: carl.wunsch@gmail.com

[¶]Massachusetts Institute of Technology and Harvard University, Cambridge Massachusetts

ABSTRACT

A dynamically consistent ocean climatology and its major temporal changes based on the years 1994-2013 has been produced from the most recent state estimate of the Estimating the Circulation and Climate of the Ocean (ECCO) project. The estimate was produced from a least-squares fit of a free running ocean general circulation model to almost all available data. Data coverage in space and time during this period is far more homogeneous than in any earlier interval and includes CTD, elephant seal, and Argo temperature and salinity profiles, the full altimetric and gravity-field coverage, satellite sea-surface temperatures, as well as the initializing meteorological coverage from the ECMWF ERA-Interim reanalysis. Dominant remaining data inhomogeneity arises from the increasing coverage from the Argo profiles beginning about 2000 to present. The state estimate exactly satisfies the free running MITgcm at all times and hence produces values satisfying the fundamental conservation laws of energy, freshwater etc., permitting its use for climate change studies. Output files are publicly available in netCDF and .mat form and include hydrographic variables, three components of velocity, and pressure as well as other variables including inferred air-sea momentum and buoyancy fluxes, 3D mixing parameters, and sea-ice cover.

1. Introduction

Climatologies, defined as temporal averages of the climate state, have been important in numerous studies. They serve as reference states for inferring changes, as initial conditions in forecasts, and sometimes as the basis of dynamical calculations. In an oceanographic context, the most widely employed global climatology has probably been the hydrographic compilation produced initially by Levitus et al. (1982) and its successors as the World Ocean Atlas (WOA). They used data from the entire history of physical oceanographic measurements of temperature and salinity as a function of horizontal position and depth. Other global averages include that of Gouretski and Koltermann (2004), using data from the World Ocean Circulation Experiment. A number of climatologies of the upper ocean are based primarily on XBT data in the early years (e.g., Ishii et al. 2003; AchutaRao et al. 2007). In related work, but with a different emphases, a number of studies of the changing ocean state have been undertaken extending back into the 19th Century (e.g., Kennedy et al. 2011).

A major issue with most such climatologies and studies based on them has been the very great inhomogeneity with which the ocean has been observed over the years (Fig. 1) and in which the filling of space and time gaps in the record has relied upon sometimes plausible, but generally untestable, statistical assumptions (see e.g., Boyer et al. 2016; Wunsch 2016). Furthermore, to our knowledge, no previous ocean climatology has comprised any variables except the hydrographic ones.

The World Ocean Circulation Experiment (WOCE) was designed in large-part to produce the first truly global, time-varying, estimate of the circulation over approximately a decade, an estimate that would be useful in defining the major climatologically important ocean elements (see Siedler et al. 2013). Until now, even the best inverse calculations (e.g., Ganachaud and Wunsch

2003; Lumpkin and Speer 2007), were forced to treat quasi-synoptic sections distributed globally over decades as though they represented a consistent time-average or, paradoxically, as a snapshot. Such assumptions ultimately are not tenable in a rapidly varying oceanic flow. The Estimating the Circulation and Climate of the Ocean (ECCO) project was formed near the start of the WOCE field program so as to address this goal using both the conventional and newly-deploying WOCE observation system, along with the rapidly advancing general circulation modelling capability (Stammer et al. 2002). This present paper is intended to introduce another climatology, based on an updated edition (Release 3; Fukumori et al. 2017) of the latest Version 4 of the ECCO ocean state estimate (Forget et al. 2015). The climatology here is focussed on the 20-year period 1994-2013, an interval in which a comparatively homogeneous set of global-scale observations were obtained so that the zero-order sampling difficulties visible in Fig. 1 are much reduced. The major inhomogeneity in the present climatology stems from the growing availability of Argo floats beginning about 2000 and extending to the present day (Roemmich et al. 2009).[1]

Essentially all of the available hydrographic data are used, including sea surface temperature products (Reynolds and Smith 1994, 1995), CTD hydrography (Talley et al. 2016), measurements from elephant seals (Roquet et al. 2013), XBTs and Argo temperature and salinity profiles (Riser et al., 2016). But *in addition,* the complete altimetric record, which begins in 1992 is employed (e.g., Fu and Cazenave 2001), as are the GRACE satellite gravity measurements (Quinn and Ponte 2008; Watkins et al. 2015), and the available a priori estimates of the meteorological forcing during the climatological interval (Dee et al. 2011, 2014).

To combine the diverse data sets including the surface forcing fields, a least-squares fit was made of a state-of-the-art ocean/sea ice general circulation model (Forget et al. 2015; cf. Marshall et al.

[1]The estimation interval begins in 1992 and extends nearly to the present time. Data observed prior to 1992 appear only tangentially in constructing first-estimate initial conditions from previous climatologies.

1997; Adcroft et al. 2004; Wunsch and Heimbach 2007, 2013; and Wunsch et al. 2009). As is done in conventional least-squares fitting, all data are weighted by the best-available estimates of their uncertainties—written as error variances or covariances. Because of the huge dimension of the resulting calculation, it is carried out by numerical iteration using Lagrange multipliers (adjoint solutions; see Wunsch and Heimbach 2013; Forget et al. 2015)).

The state estimate over the 20 years is obtained from the *free-running* ECCO configuration of the MITgcm, started from the adjusted initial conditions and mixing coefficients, and subject to the adjusted meteorological forcing fields. Time-step of the model is 1 hour over the interval 1992-2015 with only the shorter interval 1994-2013 used in the present climatology. As the product of a GCM, one generally reproducing within error estimates all of the data used, the state estimate includes values of the three-dimensional time-varying velocity field, the surface elevation and its changes, bottom pressure, ice-cover, as well as the parameters representing the non-resolved eddy-mixing via the bolus transport, the Gent and McWilliams (1990), and related schemes. Also included are the misfit fields to the different data sets used as constraints. As fitting iterations continue, new data are added, the duration increases, and the model continues to develop, the climatology changes, although at this stage, future changes are expected to be quantitatively small in most aspects.

In specific contrast to what are usually called "reanalysis products," the state estimate satisfies all of the conventional conservation requirements for any dynamically consistent climate component, including energy, heat, freshwater, vorticity—up to the accuracy of the general circulation model equations. Although considerable extra computation is required to obtain dynamically consistent solutions, no artificial interior sources and sinks appear (Wunsch and Heimbach 2013; Stammer et al. 2016) thus permitting study of changes in energy, heat-content, etc.

2. Basic Fields

A description of the time-varying three-dimensional global oceanic state and its interpretation is a forbidding undertaking. What is intended here is to call attention to the availability of fields useful for a great variety of purposes, explain how to obtain the fields in simple ways, and to invite the use and critique of the result by the wider community. Because of the great number of properties of interest in the ocean, a more elaborate pictorial description has been posted with links from the ECCO website, at the present moment in two distinct Parts. Part 1 (ECCO Consortium 2017a; ECCO2017a) is devoted to the hydrographic and derived fields such as surface elevation and mixed-layer depths. Part 2 (ECCO Consortium 2017b; ECCO2017b) focusses on the flow fields and meteorological variables. Intended for later parts are discussions of the adjoint model (the Lagrange multipliers and sensitivities), and a formal analysis of the uncertainties. Fukumori et al. (2017) described the major changes from earlier ECCO estimates.

Model output fields are available as monthly averages 1992-2015 in netCDF form at (http://mit.ecco-group.org/opendap/diana/h8_i48/contents.html or ftp://ecco.jpl.nasa.gov/Version4/Release3/). In the spirit of a climatology, and in the interests of an easily workable volume of numbers, the discussion here is limited to the 20-year average, the 20-year average months (January, February,...), the 20-year average seasonal cycle (JJA, etc.), and the yearly averages 1994, 1995,...,etc. all of which are available as MATLAB® .mat and netCDF files.

Only a few representative fields are shown here and with a few applications chosen to portray some of the more interesting or useful products. Additional fields and products can be seen in the online documents or in the many references given there. None of these results should be regarded as definitive; they are presented chiefly as an invitation to any interested scientist to recompute them as desired with different assumptions, averaging, etc.

The model native grid is shown in Figs. 2, 3 taken from Forget et al. (2015). Eddy fields are necessarily parameterized and not resolved. As Forget et al. (2015) discuss, at high northern latitudes a distorted grid is used to avoid the polar singularity. Complexity of the high latitude gridding is one of the motivations for producing this easier-to-use climatology. In some cases for scalar fields, an interpolation to a simple latitude/longitude grid has been used here for mapping purposes. For vector fields, such as the horizontal flow (u, v), or the vector wind-stress (τ_x, τ_y), the northern-most polar region has been omitted here, as its quantitative employment involves special interpolation and potential loss of accuracy. Display of fields on the native grid, including high latitudes, can be seen in the various references and on the ECCO website. High latitudes have also been omitted here in some cases where the presence of seasonal or permanent ice complicates the interpretation (e.g., salinity budgets). A specific high-northern-latitude version of the state estimate and its corresponding climatology is in preparation (A. Nguyen, personal communication 2017). Elsewhere longitudes are uniformly spaced at 1° and latitudes telescope toward the equator and pole as shown in Fig. 3. Over most of the oceanic domain, grid latitude distances maintain nearly constant grid areas.

a. Hydrography

Potential Temperature

An example of a twenty-year average hydrographic section is shown in Fig. 4 and which can be compared to the nearby quasi-synoptic WOCE section in Fig. 5. The gross structures are identical, but the average field is considerably smoother than is the WOCE section. (Color coding of the state estimate products often follows that suggested by Thyng et al. (2017) to both accommodate color-blind readers and to avoid inadvertent emphasis of some features.) Because the data used to produce the WOCE Atlases (http://woceatlas.ucsd.edu/; and see Schlitzer, 2017) were also used in the state estimate, large-scale gross structures in the ocean circulation can be seen readily in the various online or printed WOCE Atlases, and so are not reproduced here.

Fig. 6 shows one example of a global thermal section at 14°N and Figs. 7, 8 are example temperatures at fixed depth levels. These and other fields are time averages consistent with the time mean flow and meteorological fields displayed below. In many but not all cases, a histogram of values is shown as an inset, with isolated outliers (usually within topographically complex areas beyond the model resolution) omitted.

Time-Dependence

Elements of the fluid ocean change constantly. As examples, Figs. 9, 10 show the estimated annual mean anomalies at 105m for two different years. Figure 11 is the 20-year average seasonal anomaly in December-January-February at 5m. The annual anomalies (not shown here) readily permit calculation of the changing heat content of the ocean over 20 years, shown as the corresponding temperature changes in levels in Fig. 12. Upper levels are noisy while the deeper ones can be interpreted as showing simple linear trends. These and other products become part of the discussion of the oceanic heat uptake, the putative slowdown in atmospheric warming ("hiatuses"), etc. (see Wunsch and Heimbach 2014; Medhaug et al. 2017; Liang et al. 2017).

Salinity

As a least-squares estimate, the ECCO state leaves explicitly computed misfits by month, year, and on the average. As an example, Fig. 13 shows the gridded 20-year mean misfit to the salinity data at 5m. Apart from outliers in the Labrador Sea and other shallow regions (see e.g., Fenty and Heimbach 2013), the observations are generally within 0.5g/kg over most of the ocean.

The time-average salinity field at one depth is shown in Fig. 14. The histogram insert shows a multi-modal distribution of values. Two 20-year average zonal sections of salinity are displayed in Figs. 15, 16 along the equator, and through the Drake Passage, respectively. A great deal of structure remains even after 20 years of averaging.

b. Pressure and Flow Fields

Surface Elevation

Surface elevation, $\eta(\theta,\lambda,t)$, relative to an estimated geoid is largely, but not completely, determined by the altimetric data: the state estimate is simultaneously being fit to meteorological forcing, the thermal, salinity and ice fields, and any other data (e.g., gravity and altimeter height changes) that are present. A full determination of which elements of which observations are controlling the field depends upon the adjoint sensitivity of estimated η to each of these data sets. The adjoint solution will be discussed elsewhere. But because the altimetric records are the only ones nearly uniform and global over the entire 20 years, the 20-year average misfit to the time-varying altimetric measurement of η is shown in Fig. 17. Apart from some isolated outliers that have been suppressed in the charts, the misfits are generally within 10cms overall, highest at high latitudes, and showing some residual structures in the tropics. Misfits associated with the moving western boundary currents also appear.

Elevation and Pressure

The time-average dynamic topography, relative to the GRACE geoid, appears in Fig. 18 and again shows the classical gyres. Its anomaly in 1998 appears in Fig. 19. It can be compared to the total flow (not just the geostrophic component) in Fig. 20. Hydrostatic pressure fields, including bottom values, are also available.

Flow-Fields

The 20-year average horizontal components of Eulerian velocity (u,v) are displayed at several depths in Figs. 21, 22. These (especially Fig. 21) include both the geostrophic and ageostrophic components. At 3600m, the influence of topography is marked.

Various velocity anomalies are available by month, year, and season. As examples Fig. 23 is the 5m anomaly in 1994, and Fig. 24 is the corresponding anomaly in 1997, the beginning year of a major El Niño. A zonal flow anomaly in 1995 in the Drake Passage is shown in Fig. 25. A very large number of such displays is possible. Anomalies 1994-2013 (not shown) have a net annual Drake Passage transport variability between -5 and +3Sv and whose values require integrating across the complex meridional structure.

The Eulerian vertical velocity, w, is a crucial element in the oceanic general circulation, especially in the vorticity balance. Fig. 26 displays the 20-year mean w pattern at 105 m, a rough equivalent to the Ekman depth. Sign changes correspond to the classical gyre circulation as well as to the intense equatorial and coastal upwelling phenomena. At great depths (not shown), the pattern rapidly becomes complex beyond simple verbal description, and particularly as topographic features are approached from above (see Liang et al. 2017a for a discussion of the bolus velocity, w_b, and its sum with w.).

Meteorological Values

Meteorological forcing variables of wind, surface air temperature, specific humidity, precipitation, and radiative fluxes from the ERA-Interim reanalysis (Dee et al. 2011, 2014) are among the prior estimates of the control variables. As is well-known from a number of comparisons with other reanalysis products (e.g., Bromwich et al. 2007, 2015), none of these values can be regarded as very accurate. Chaudhuri et al. (2013, 2016), have discussed the errors that are assigned to them). In the process of determining the state estimate, these meteorological fields are adjusted so that the subsequent calculation with the free-running model, using the modified controls, renders it consistent with the ocean data. In general, the adjustments to the controls are small (see Fig. 27). Although the adjustments must be interpreted in terms of the directions of the originating means, a general result is a strengthening of the zonal winds both in the regions of high latitude westerlies and lower latitude easterlies. The adjustments in τ_x are skewed towards positive values, while the meridional ones (not shown) are more symmetric and weaker.

The estimated wind stress along with the surface flows permits calculation of the rate of working of the wind on the ocean circulation. Because, like the heat and freshwater transports, it depends upon second order products $\langle \mathbf{v} \cdot \boldsymbol{\tau} \rangle$, only the map of $\langle u \rangle \langle \tau_x \rangle$ is displayed as an example (Fig. 28).[2]

Mixed-Layer Depth

The oceanic mixed-layer depth is a function both of the meteorology and oceanic dynamics. Using the Kara et al. (2000, 2003) definition based on density changes, Fig. 29 displays the 20-year mean mixed-layer depth. As expected (not shown), considerable seasonal changes exist in these values.

3. Dynamics

A full discussion of oceanic circulation dynamics is far beyond the intended scope of this overview. As one example of possibilities, Fig. 30 displays a Rossby number, $Ro = UL/f$ at 400m, where a fixed value of $L = 100$km is used with the 20-year average horizontal speed. Apart from the equator, where it is not a useful measure of flow linearity, values are generally below $Ro = 0.06$, consistent with linear dynamics. Other Rossby number definitions can be used (e.g., vorticity).

[2] A full discussion of the rates of wind work requires strong assumptions about the averaging interval chosen for values, hourly, monthly, annual, etc. and is not pursued here.

A second example is shown in Fig. 31 as the 20-year average angle between the ageostrophic component of the surface flow and the 20-year average wind stress. With some exceptions, the estimated angle is not far from the canonical $\pm 45°$, changing sign across the equator. In the southern hemisphere, the most probable angle is -55°, and in the northern hemisphere it is 66°. The ageostrophic flow was calculated as the the 5m total flow minus the geostrophic component from the mean dynamic topography in Fig. 18. A number of assumptions go into the calculation of the conventional 45°, including accuracy of the stress estimate, having the true surface velocity, and the nature of the turbulence within the Ekman-like layer.

Eddy physics, in the form of bolus velocities and vertical and horizontal mixing coefficients and viscosities can also be discussed using state-estimate products. These will be displayed and described more fully elsewhere.

4. Regional Studies

Regional oceanographic subsets are easily extracted from the global files as annual, seasonal etc., averages. A very large number of interesting regional studies is possible, bearing in mind the resolution questions near boundaries. As an example of what can be done regionally with salinity, Fig. 32 displays the twenty-year seasonal average anomalies at 5m depth of salinity in the Bay of Bengal (see e.g.,the special issue *Oceanography*, 29(2), 2016) for a comparison).

5. Final Remarks

The gist of this paper is that understanding the ocean either as an instantaneous picture, or as an average over any finite period, must confront the inescapable fact that the system is intensely time-varying. Significantly improving the accuracy of the estimates made from the present data sets, if interpreted as climatological averages, will not be easy, involving as it does the need for far longer records, much better coverage of the ocean below 2000m, and in specific regions, improved time-space resolution both of the observations and of the underlying general circulation model. Better quantification of the error structures of all existing and future data sets is also very important.

6. Obtaining the State Estimate Values

A concise documentation of ECCO Version 4 Release 3 is given by Fukumori et al. (2017). The full state estimate values on the model native grid at monthly intervals from 1992-2015 are available at ftp://ecco.jpl.nasa.gov/Version4/Release3/ in netCDF form and which includes the full suite of data used in the least-squares fitting. A subset of values making up the present climatology described here, 1994-2013, as described in ECCO Consortium (2017a,b) in MATLAB® .mat files, can be found at http://mit.ecco-group.org/opendap/diana/h8_i48/. Additional documentation is available that describes how to analyze property budgets using these estimates (Piecuch 2017) and how to run the model to produce additional fields not available in the archive (Wang 2017). Any of the authors can be contacted for help and advice. Comments about difficulties or errors are welcomed.

Acknowledgments. ECCO has been funded over many years primarily by the National Aeronautics and Space Administration at MIT, AER, and JPL. Particular thanks are owed the NASA Program Manager, Eric Lindstrom, for his sustained support and advice.

References

AchutaRao, K. M., and Coauthors, 2007: Simulated and observed variability in ocean temperature and heat content. Proc. Nat. Acad. Scis., USA, 104, 10768-10773.

Adcroft, A., C. Hill, J. M. Campin, J. Marshall, and P. Heimbach, 2004: Overview of the formulation and numerics of the MIT GCM, ECMWF Proceedings, Shinfield Park, Reading UK, 139-150 pp., http://gfdl.noaa.gov/˜aja/papers/ECMWF–2004-Adcroft.pdf.

Boyer, T., and Coauthors, 2016: Sensitivity of global upper-ocean heat content estimates to mapping methods, XBT bias corrections, and baseline climatologies. J. Clim. , 29, 4817-4842.

Bromwich, D. H., Fogt, R. L., Hodges, K. I.,Walsh, J. E., 2007: A tropospheric assessment of the ERA-40, NCEP, and JRA-25 global reanalyses in the polar regions. J. Geophys. Res.-Atm., 112.

Bromwich, D. H., Wilson, A. B., Bai, L.-S., Moore, G. W. K., & Bauer, P., 2015: A comparison of the regional Arctic System Reanalysis and the global ERA-Interim Reanalysis for the Arctic. Quat. J. Roy. Met. Soc., 142(695), 644–658. http://doi.org/10.1002/qj.2527

Chaudhuri, A. H., R. M. Ponte, and G. Forget, 2016: Impact of uncertainties in atmospheric boundary conditions on ocean model solutions. Ocean Mod., 100, 96-108.

Chaudhuri, A. H., R. M. Ponte, G. Forget, and P. Heimbach, 2013: A comparison of atmospheric reanalysis surface products over the ocean and implications for uncertainties in air-sea boundary forcing. J. Clim. , 26, 153-170.

ECCO Consortium (ECCO2017a), 2017a: A Twenty-Year Dynamical Oceanic Climatology: 1994-2013. Part 1: Active Scalar Fields: Temperature, Salinity, Dynamic Topography, Mixed-Layer Depth, Bottom Pressure. (MIT DSpace), http://hdl.handle.net/1721.1/107613

——— (ECCO2017b), 2017b: A Twenty-Year Dynamical Oceanic Climatology: 1994-2013. Part 2: Velocities and Property Transports. (MIT DSpace), http://hdl.handle.net/1721.1/109847.

Dee, D. P., M. Balmaseda, G. Balsamo, R. Engelen, A. J. Simmons, and J. N. Thépaut, 2014: Toward a consistent reanalysis of the climate System. Bull. Am. Met. Soc., 95, 1235-1248.

Dee, D. P., and Coauthors, 2011: The ERA-Interim reanalysis: configuration and performance of the data assimilation system. Quat. J. Roy. Met. Soc., 137, 553-597.

Fenty, I., and P. Heimbach, 2013: Coupled sea-ice-ocean-state estimation in the Labrador Sea and Baffin Bay. J. Phys. Oc., 43, 884-904.

Forget, G., D. Ferreira, and X. Liang, 2015: On the observability of turbulent transport rates by Argo: supporting evidence from an inversion experiment. Ocean Sci, 11, 839-853.

Forget, G., J.-M. Campin, P. Heimbach, C. Hill, R. Ponte, and C. Wunsch, 2015: ECCO version 4: an integrated framework for non-linear inverse modeling and global ocean state estimation. Geosci. Model Dev., 8, 3071-3104.

Fu, L.-L., and E. A. Cazenave, 2001: Satellite Altimetry and Earth Sciences. A Handbook of Techniques and Applications. Academic, San Diego, 463 pp.

Fukumori, I., O. Wang, I. Fenty, G. Forget, P. Heimbach, and R. Ponte, 2017: ECCO Version 4 Release 3. ftp://ecco.jpl.nasa.gov/Version4/Release3/doc/v4r3_summary.pdf.

Ganachaud, A., & Wunsch, C., 2000:. Improved estimates of global ocean circulation, heat transport and mixing from hydrographic data. Nature, 408(6811), 453-457. http://doi.org/-10.1038/35044048.

Gent, P. R., and J. C. Mcwilliams, 1990: Isopycnal mixing in ocean circulation models. J. Phys. Oc., 20, 150-155.

Gouretski, V. V.,. Koltermann, K. P., 2004: WOCE Global Hydrographic Climatology., Berichte des Bundesamtes für Seeschifffahrt und Hydrographie Nr. 35/2004, Hamburg and Rostock, 50 pp.

Ishii, M., Kimoto, M., & Kachi, M., 2003:. Historical ocean subsurface temperature analysis with error estimates. Mon. Weath. Rev., 131(1), 51–73. http://doi.org/10.1175/1520-0493(2003)131.

Kara, A. B., P. A. Rochford, and H. E. Hurlburt, 2000: An optimal definition for ocean mixed layer depth, J. Geophys. Res., 105(C7), 16803–16821, doi:10.1029/2000JC900072 http://doi.org/10.1002/qj.2527

Kara, A. B., P. A. Rochford, and H. E. Hurlburt, 2003: Mixed layer depth variability over the global ocean. J. Geophys. Res., 108, 3079.

Kennedy, J. J., N. A. Rayner, Smith, R. O., D. E. Parker, and M. Saunby, 2011: Reassessing biases and other uncertainties in sea surface temperature observations measured in situ since 1850: 2. Biases and homogenization. J. Geophys. Res., 116.

Knudsen, P., and R. Bingham, Andersen, O., Rio, M. H., 2011: A global mean dynamic topography and ocean circulation estimation using a preliminary GOCE gravity model. J. Geod., 85, 861-879.

Koltermann, K. P., V. V. Gouretski, and K. Jancke, Eds., 2011: Hydrographic Atlas of the World Ocean Circulation Experiment (WOCE). Volume 3: Atlantic Ocean International WOCE Project Office, Southampton, UK, ISBN 090417557X.

Levitus, S., 1982: Climatological Atlas of the World Ocean, 173 pp plus microfiche NOAA Professional Paper 13.

Liang, X., C. Wunsch, P. Heimbach, and G. Forget, 2015: Vertical redistribution of oceanic heat content. J. Clim., 28, 3821-3833, 2550-2562

Liang, X., C. G. Piecuch, R. M. Ponte, G. Forget, C. Wunsch, P. Heimbach, 2017a: Change of the global ocean vertical heat transport over 1993-2010. Submitted for publication.

Liang, X. C. Wunsch, M. Spall, 2017b: Global ocean vertical velocity from a dynamically consistent ocean state estimate, Submitted for publication.

Lumpkin, R. and K. Speer, 2007: Global ocean meridional overturning, J. Phys. Oc., 37,, 2550-2562.

Marshall, J., A. Adcroft, C. Hill, L. Perelman, and C. Heisey, 1997: A finite-volume, incompressible Navier Stokes model for studies of the ocean on parallel computers. J. Geophys. Res.-Oceans, 102, 5753-5766.

Maximenko, N., and Coauthors, 2009: Mean dynamic topography of the ocean derived from satellite and drifting buoy data using three different techniques. J. Atm. Oc. Tech., 26, 1910-1919.

Medhaug, I., Stolpe, M. B., Fischer, E. M., & Knutti, R., 2017:. Reconciling controversies about the "global warming hiatus." Nature, 545(7652), 41–47. http://doi.org/10.1038/nature22315

Piecuch, C. G., 2017:, A note on evaluating budgets in ECCO Version 4 Release 3. ftp://ecco.jpl.nasa.gov/Version4/Release3/doc/evaluating_budgets_in_eccov4r3.pdf.

Quinn, K. J., and R. M. Ponte, 2008: Estimating weights for the use of time-dependent gravity recovery and climate experiment data in constraining ocean models, J. Geophys. Res., 113, C12013, doi:10.1029/2008JC004903.

Roemmich, D., and Coauthors, 2009: The Argo Program: Observing the global ocean with profiling floats. Oceanog., 22, 34-43.

Reynolds, R. W. and Smith, T. M., 1994. Improved global sea surface temperature analyses using optimum interpolation. J. Clim., 7, 929-948.

Reynolds R. W. and Smith, T. M., 1995: A high resolution global sea-surface climatology. J. Clim., 8, 1571-1583.

Riser, S. C., Freeland, H. J., Roemmich, D., Wijffels, S., Troisi, A., Belbéoch, M., et al., 2016:. Fifteen years of ocean observations with the global Argo array. Nature Clim. Change, 6(2), 145–153. http://doi.org/10.1038/nclimate2872

Roquet, F., Wunsch, C., Madec, G., 2011: On the patterns of wind-power input to the ocean circulation. J. Phys. Oc., 41, 2328-2342.

Roquet, F., and Coauthors, 2013: Estimates of the Southern Ocean general circulation improved by animal-borne instruments. Geophys. Res. Letts., 40, 6176-6180.

Schlitzer, R., 2017: Ocean Data View, odv.awi.de,.

Siedler, G., S. Griffies, Gould, J., Church, J. , Eds., 2013: Ocean Circulation and Climate, 2nd Ed. A 21st century perspective. Academic Press.

Stammer, D., C. Wunsch, R. Giering, C. Eckert, P. Heimbach, J. Marotzke, A. Adcroft, C. Hill, J. Marshall, 2003: Volume, heat and freshwater transports of the global ocean circulation 1992-1997, estimated from a general circulation model constrained by WOCE data. J. Geophys. Res., 107, C9.

Stammer, D., and Coauthors, 2002: Global ocean circulation during 1992-1997, estimated from ocean observations and a general circulation model. J. Geophys. Res.-Oceans, 107, C9

Stammer, D., Balmaseda, M., Heimbach, P., Köhl, A., & Weaver, A., 2016:. Ocean data assimilation in support of climate applications: Status and perspectives. Ann. Rev. Mar. Sci., 8, 491–518. http://doi.org/10.1146/annurev-marine-122414-034113

Talley, L. D., and Coauthors, 2016: Changes in ocean heat, carbon content, and ventilation: A review of the first decade of GO-SHIP Global Repeat Hydrography. Ann. Rev. Mar. Sci., Vol 8, 185-215.

Thyng, K. M., C. A. Greene, R. D. Hetland, H. M. Zimmerle, and S. F. DiMarco, 2016: True colors of oceanography. Guidelines for effective and accurate colormap selection. Oceanog., 29, 9-13.

Wang, O., 2017: Instructions for reproducing ECCO Version 4 Release 3. ftp://ecco.jpl.nasa.gov/Version4/Release3/doc/ECCOv4r3_reproduction.pdf.

Watkins, M. M., Wiese, D. N., Yuan, D.-N., Boening, C., & Landerer, F. W., 2015: Improved methods for observing Earth's time variable mass distribution with GRACE using spherical cap mascons. J. Geophys. Res.: Solid Earth, 120(4), 2648–2671. http://doi.org/10.1002/-2014JB011547

Wunsch, C., 1998: The work done by the wind on the oceanic general circulation. J. Phys. Oc., 28, 2332-2340.

Wunsch, C., 2016: Global ocean integrals and means, with trend implications. Ann. Rev. Mar. Sci., Vol 8, C. A. Carlson, and S. J. Giovannoni, Eds., 1-33.

Wunsch, C., and P. Heimbach, 2007: Practical global oceanic state estimation. Physica D-Nonlin. Phen., 230, 197-208.

——, 2013: Dynamically and kinematically consistent global ocean circulation state estimates with land and sea ice. Ocean Circulation and Climate, 2nd Edition, J. C. G. Siedler, W. J. Gould, S. M. Griffies, Eds., Ed., Elsevier, 553-579.

Wunsch, C., P. Heimbach, R. M. Ponte, I. Fukumori, and ECCO Consortium Members, 2009: The global general circulation of the ocean estimated by the ECCO-Consortium. Oceanog., 22, 88-103.

Zhai, X. M., and H. L. Johnson, Marshall, D. P., Wunsch, C., 2012: On the wind power input to the ocean general circulation. J. Phys. Oc., 42, 1357-1365.

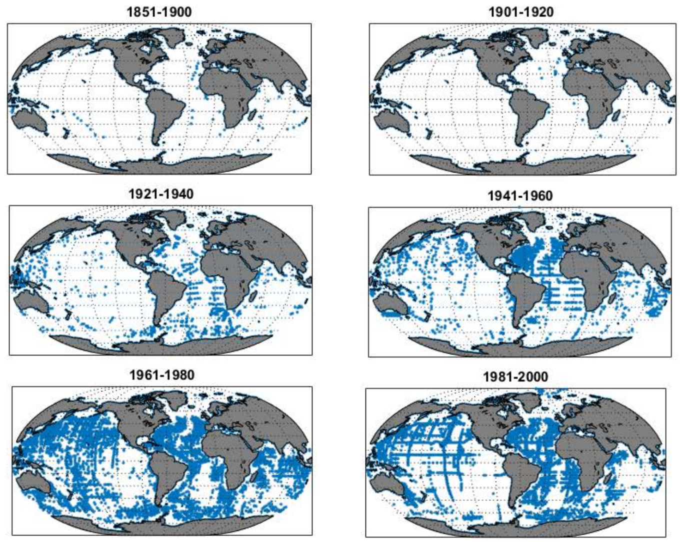

FIG. 1. Hydrographic measurements reaching at least 3600m between (a) 1851 and 1900, and then in 20-year increments to 2000. From WOA. See Wunsch (2016) for corresponding data distributions to 2000m. Early years have a North Atlantic bias, and all years have seasonal biases (not shown) towards low latitudes in winter. Although crude spatial averages could have been formed as early as 1900, even in later decades their accuracy would have been poor. In some cases, shallow topographic features such as the mid-ocean ridges are apparent as blank spaces (e.g., the North Atlantic 1941-1960).

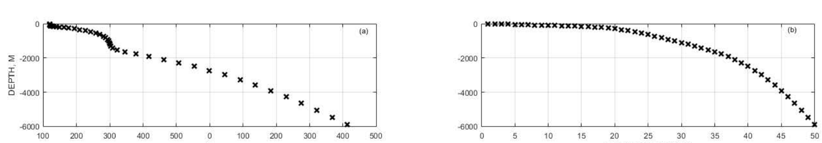

FIG. 2. (a) Level thicknesses; (b) level depths in the ECCO version 4 state estimate. (From Forget et al., 2015).

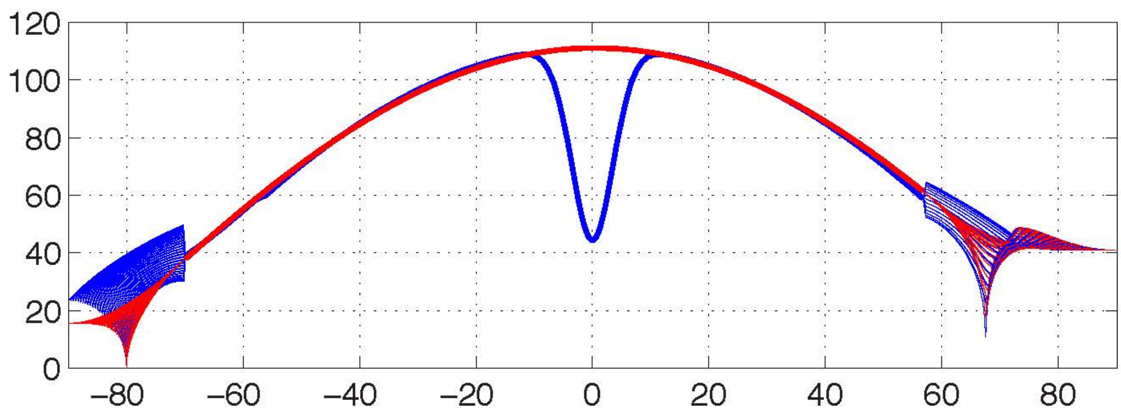

FIG. 3. Latitude (blue curve) and longitude spacing in kilometers as a function of latitude (from Forget et al., 2015). Closer latitude spacing exists near the equator. At high latitudes the complex grid leads to a distribution of spacings (see Figs. 1,2 of Forget et al., 2015). Most of the high latitude southern region is land. At mid-latitudes, horizontal cell areas are nearly constant.

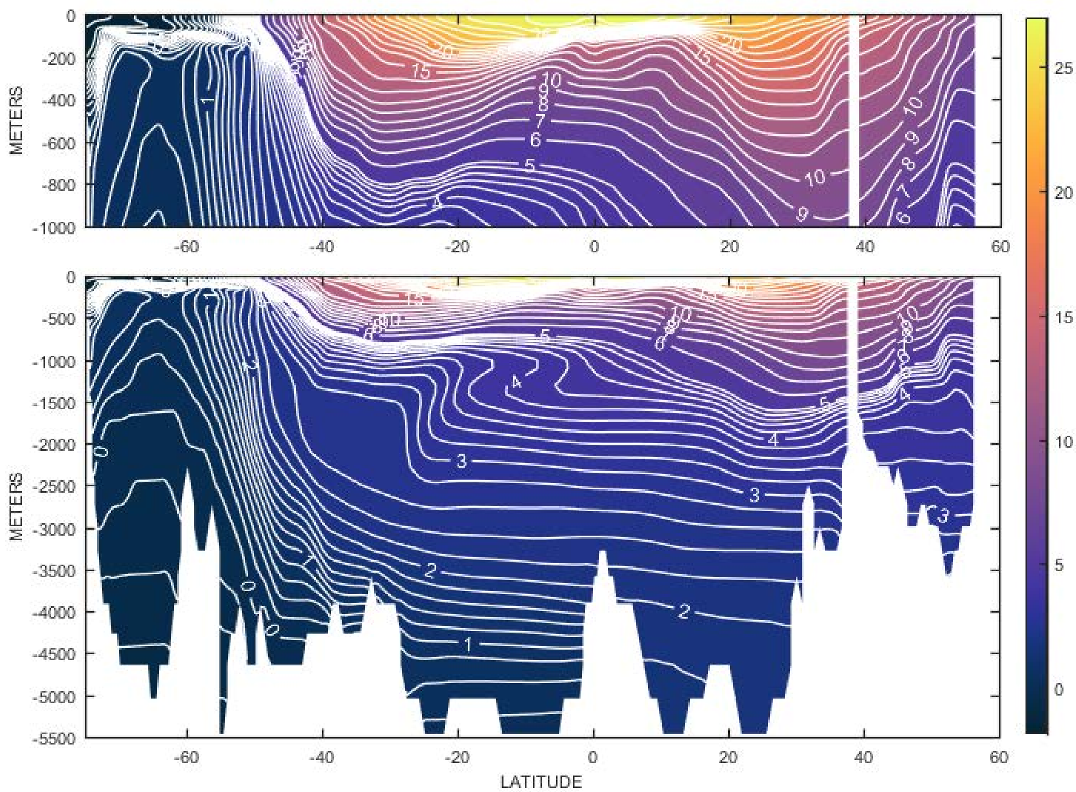

FIG. 4. Twenty-year mean section of potential temperature (°C) down 29°W in the Atlantic ocean. The section is smoother than any quasi-synoptic section would be, although considerable structure remains despite the averaging time.

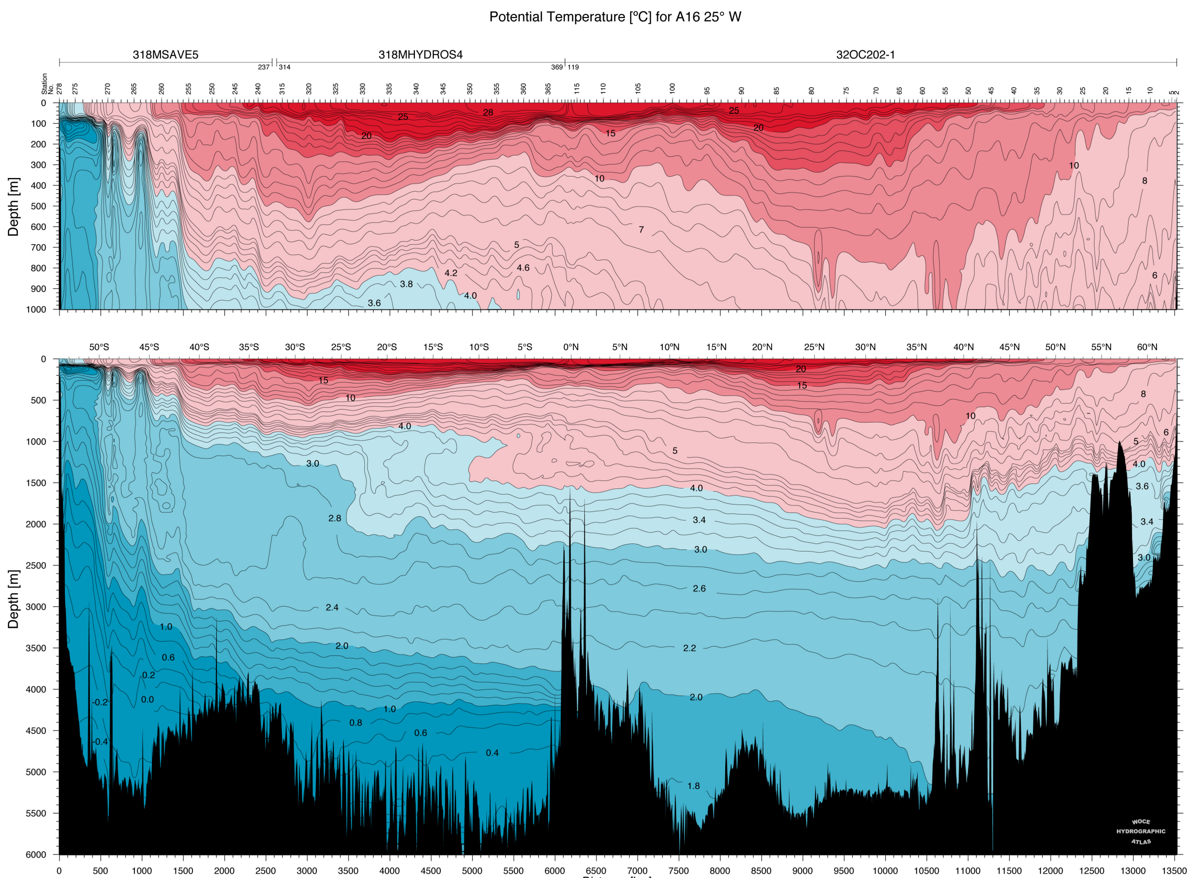

FIG. 5. WOCE section of temperature (°C) nominally down 25°W in the Atlantic Ocean. From Koltermann et al. (2011). Color coding is conventional. Notice the presence of much small scale structure of several degrees of latitude not present in the 20-year mean section.

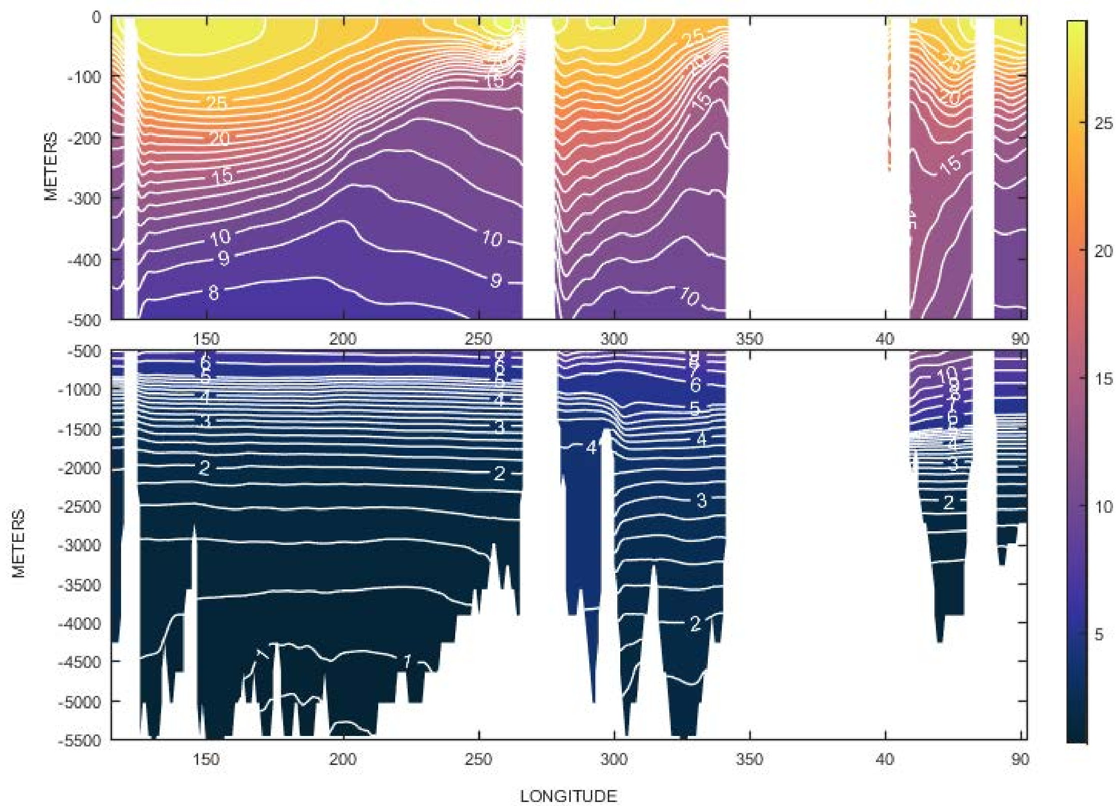

FIG. 6. Twenty-year mean potential temperature in all three oceans along 14°N.

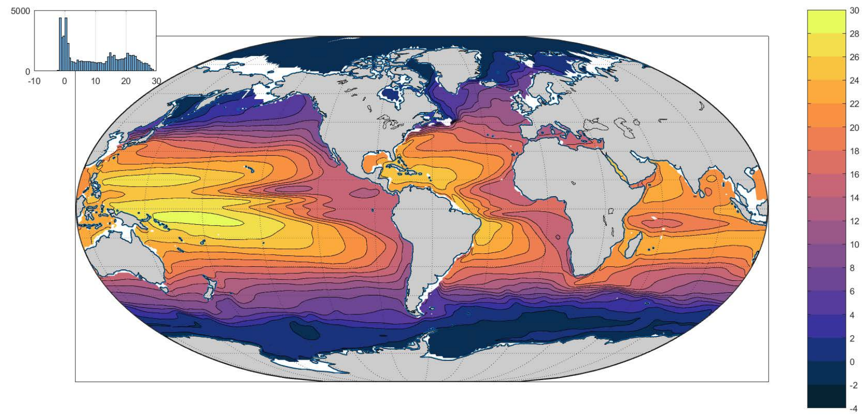

FIG. 7. Twenty-year average potential temperature at 105m (°C). Inset shows the histogram of values at this depth.

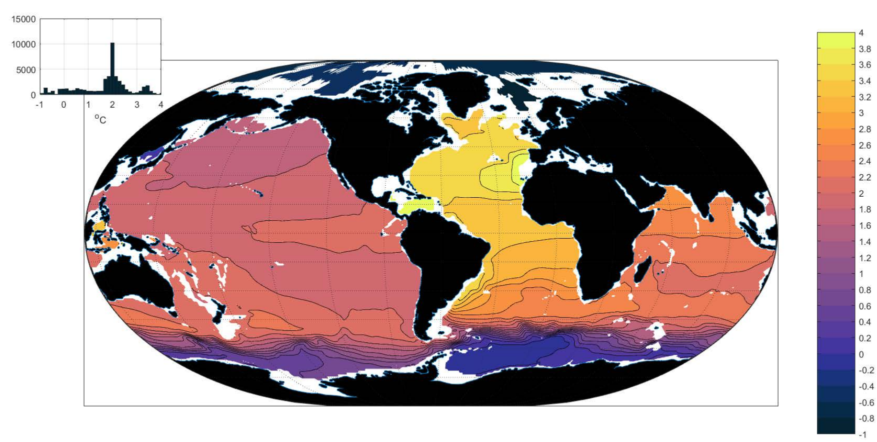

FIG. 8. Twenty-year average temperature at 2084m (°C). Color saturates at 3.9 °C with outlier maxima occurring in the Mediterranean and Gulf of Mexico where the deep water resolution is inadequate for the topography.

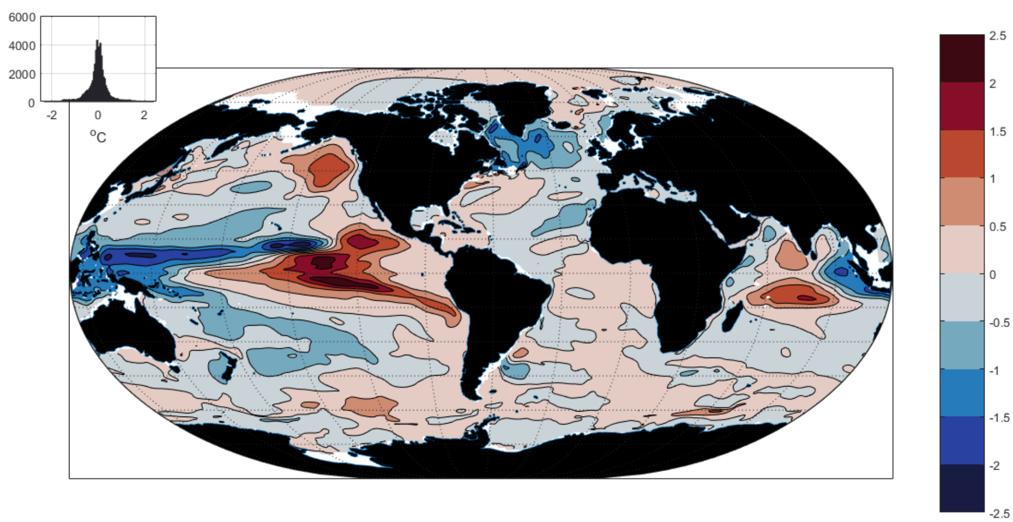

FIG. 9. Anomaly of temperature (°C) in 1994 relative to the 20 year mean at 105m.

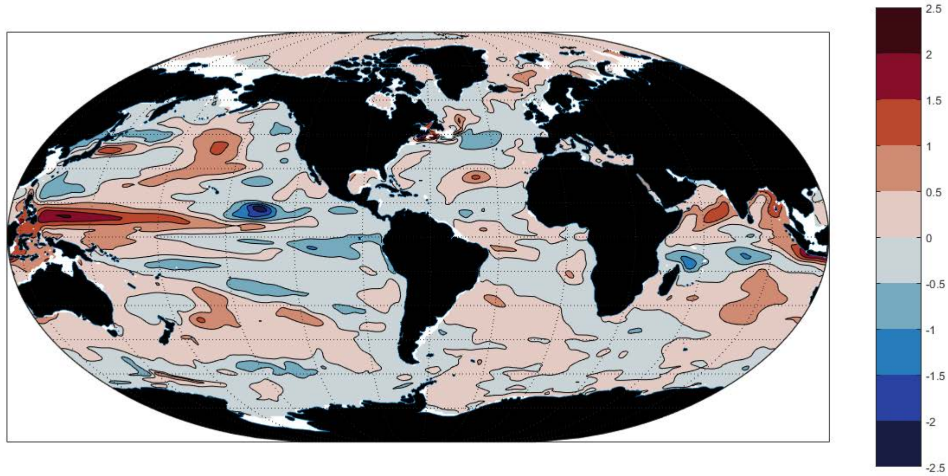

FIG. 10. Annual mean anomaly of temperature at 105m in 2013, twenty-years after that in Fig. 9.

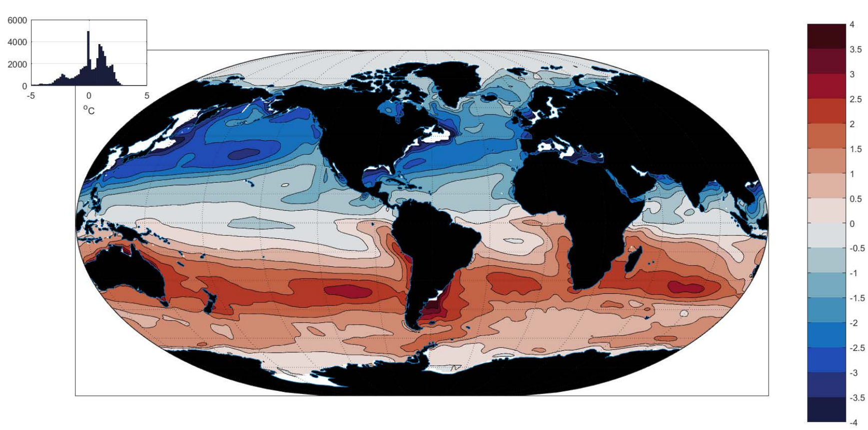

FIG. 11. Example of a 20-year average seasonal (December, January, February, DJF) mean 5m temperature (°C) anomalies. The main feature is the interhemispheric anti-symmetry with the conventional larger amplitudes in the northern region.

FIG. 12. Volume weighted temperature change C by year. Upper panel is the average to 100m, 700m, and the total, top-to-bottom. Lower panel shows the averages to 3600m, the repeated total top-to-bottom, and the abyssal layer below 3600m which shows net cooling.

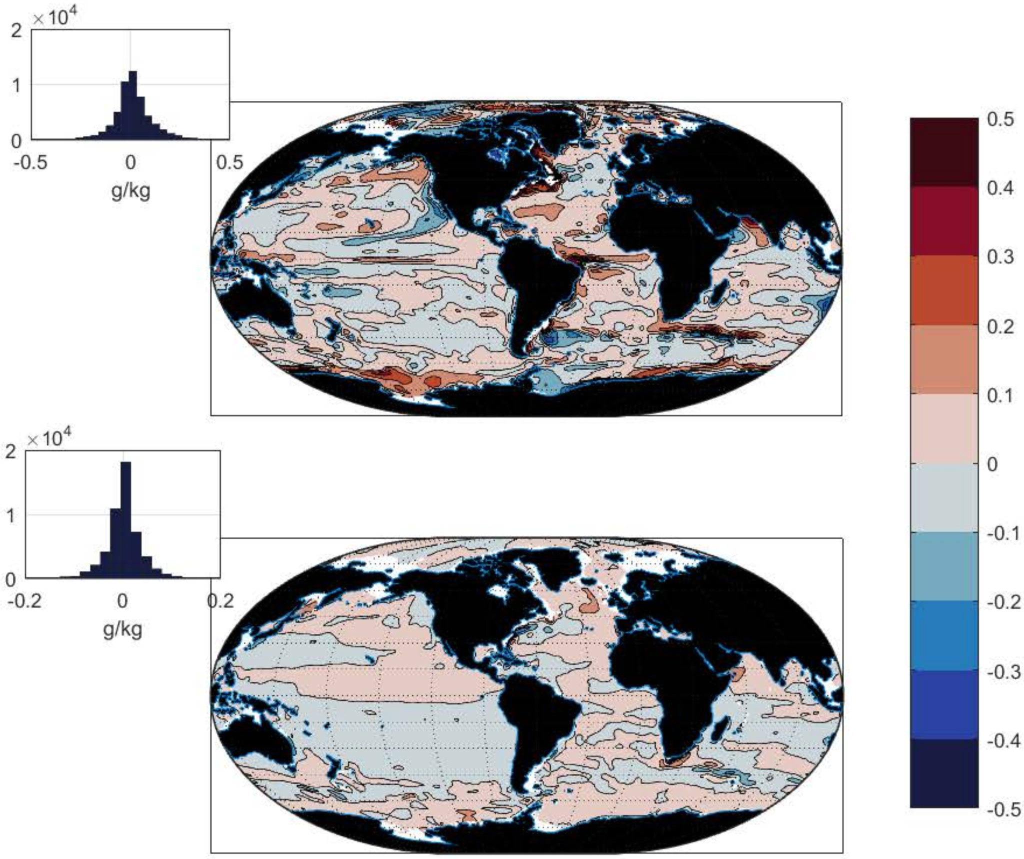

FIG. 13. (Upper panel) Misfit of the state estimate to the salinity data (g/kg) averaged over 20 years at 105m. Histogram inset shows the distribution of values which is unimodal about 0 g/kg and close to Gaussian and thus consistent with near-normality an a priori hypothesis. Some isolated outliers are omitted. (Lower panel). Same as upper panel except at 552 m. Although not tested, the residuals have a visual resemblance to a stochastic field with regional variations.

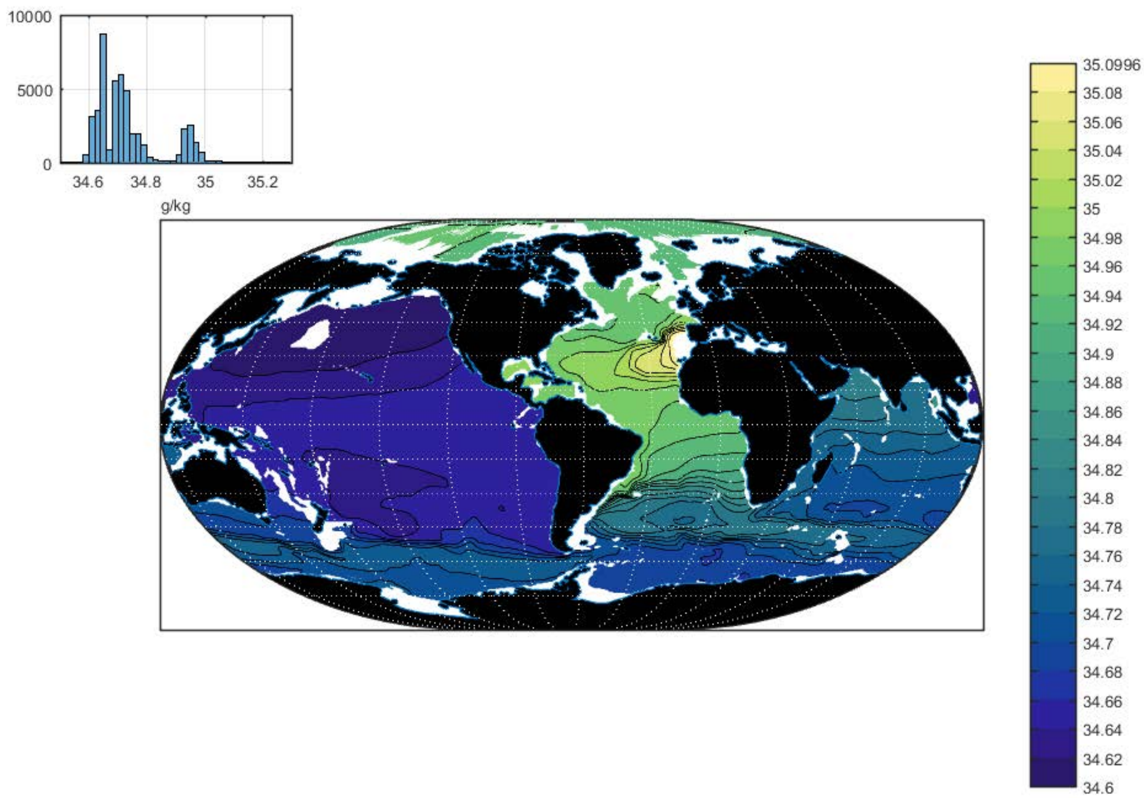

FIG. 14. Twenty-year average salinity (g/kg) at 2100m. Excess values in the North Atlantic and the extreme of the Mediterranean Sea outflow (Mediterranean Sea values are truncated here) are visible. The relatively saline Atlantic and fresh Pacific Oceans are apparent.

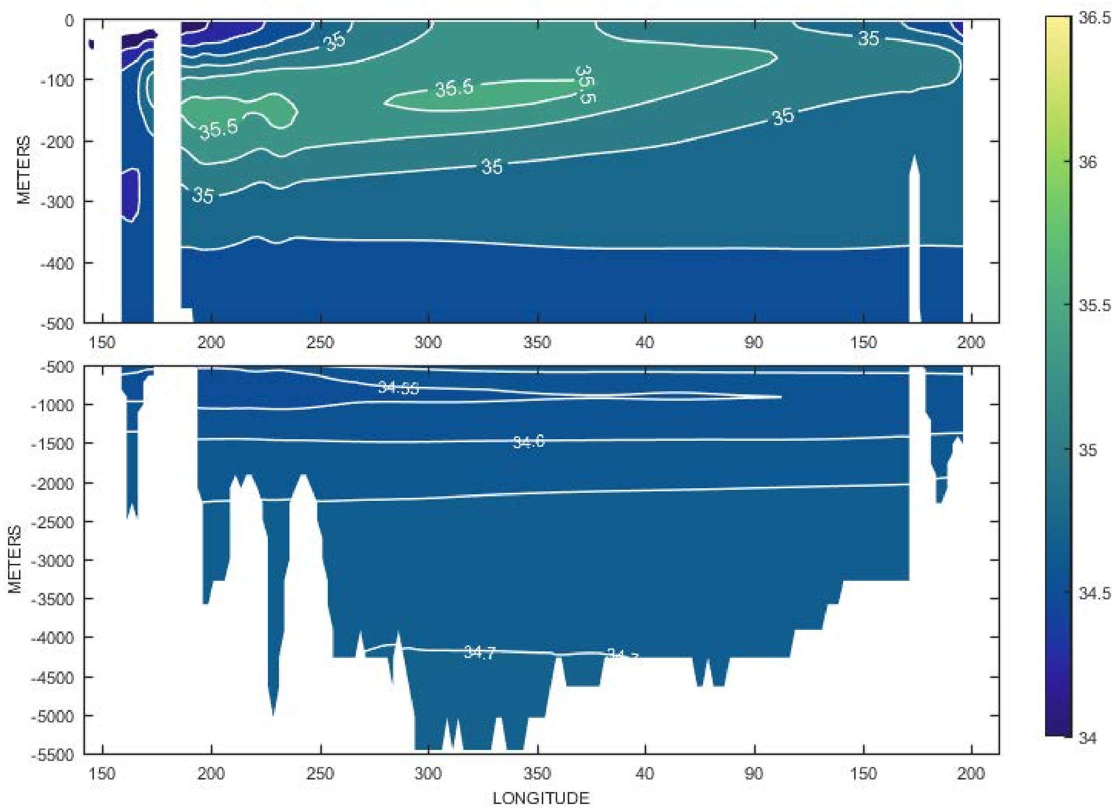

438 FIG. 15. Twenty-year average salinity, g/kg, in a zonal section along the equator in the Pacific Ocean. Note extra contours below 500m.

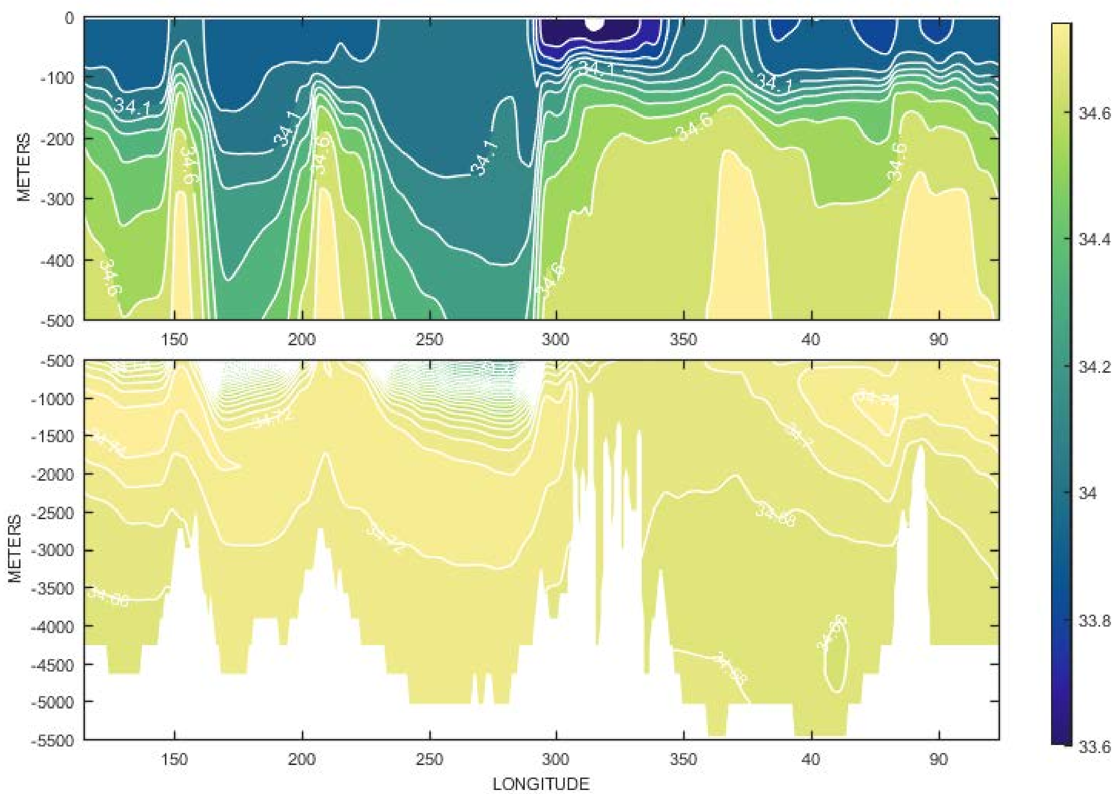

FIG. 16. Twenty-year mean salinity in a zonal section through the Drake Passage (60°S) with a complex zonal structure as seen also in temperature (not shown here; see ECCO2017a) and producing a similarly complex zonally varying $T-S$ relationship in the Southern Ocean.

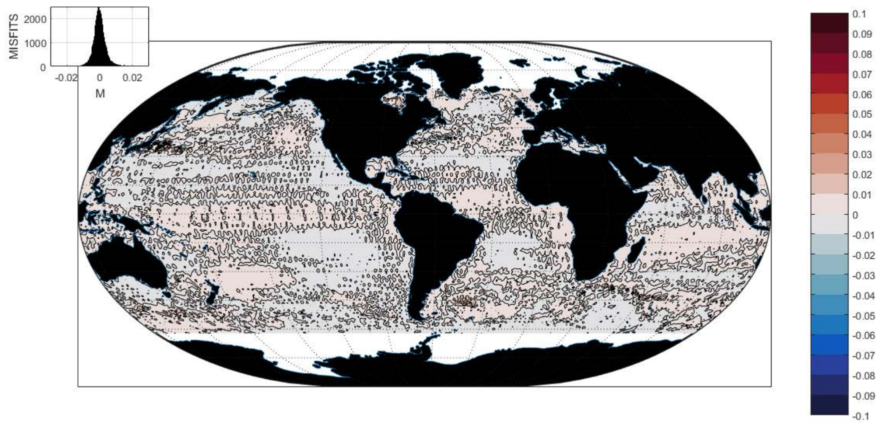

FIG. 17. Average misfit (m) over 20 years of the state estimated values of η and that measured by the suite of altimeters. Based upon the average of the monthly misfits in the generally ice-free region. Weighting operators were chosen so that small scale features are ignored in the least-squares fitting, as they are dominated by geoid error and mesoscale features. Unimodality-about-zero character of the residuals is clear, but large-scale patterns suggest residual systematic errors in the altimeter data or in the model of order 2cm. Complex detail of the zero contour, which dominates the plot, is consistent with a zero-mean, nearly random, residual.

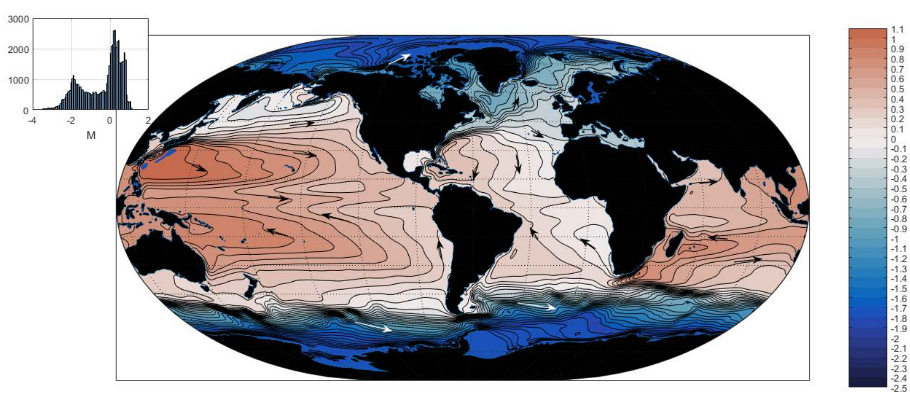

FIG. 18. Twenty-year mean dynamic topography (m). Lowest values occur in the ice-covered areas. Offsetting the entire surface by a constant would have no observable dynamical consequences. Compare to Maximenko et al. (2009), Knudsen et al. (2011). Inset shows the histogram of values about the mean. The overall magnitude is about 3m.

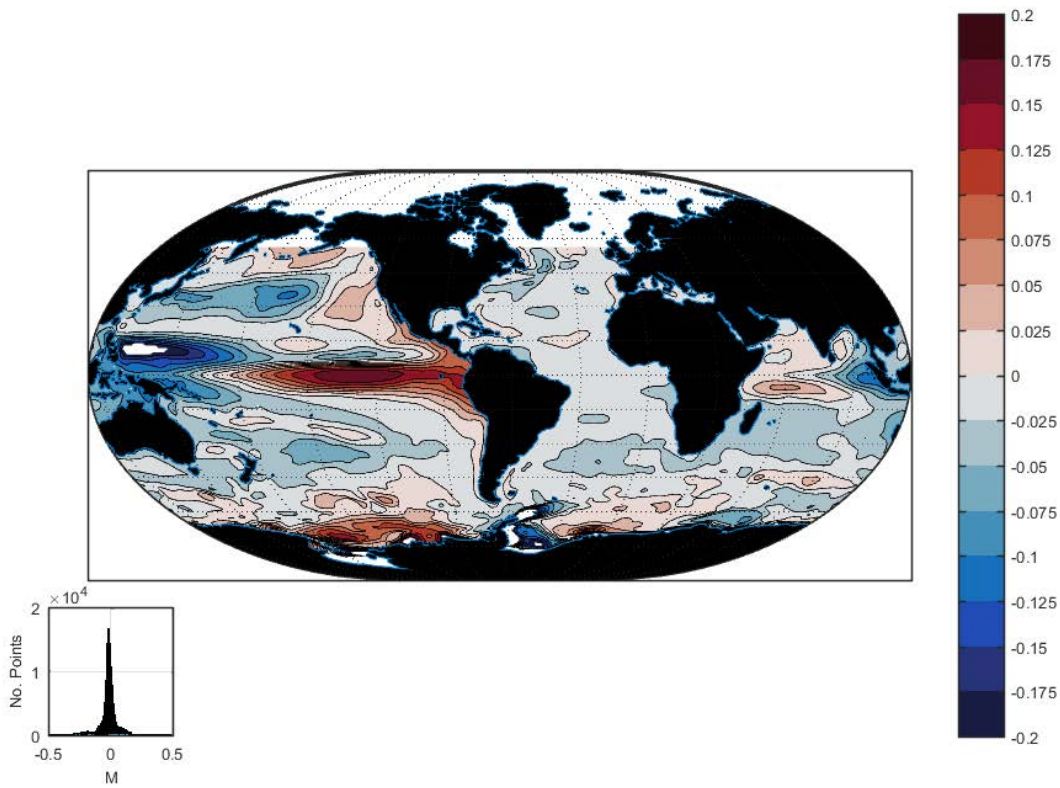

FIG. 19. Average of the anomaly of η (m) during El Niño year (1998).

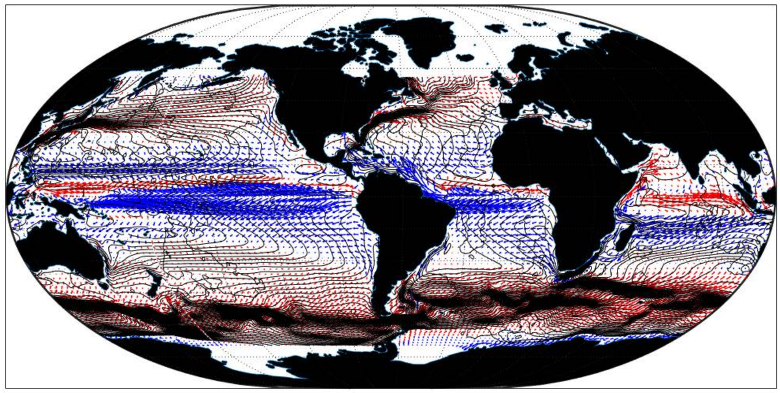

FIG. 20. Twenty-year average flow at 5m depth. Largest flow is 53 cm/s. Red arrows have an eastward component, blue a westward one. The dynamic topography from Fig. 18 is superimposed. Deviation of the flow from the elevation contours is the ageostrophic flow. Polar regions under ice are not shown.

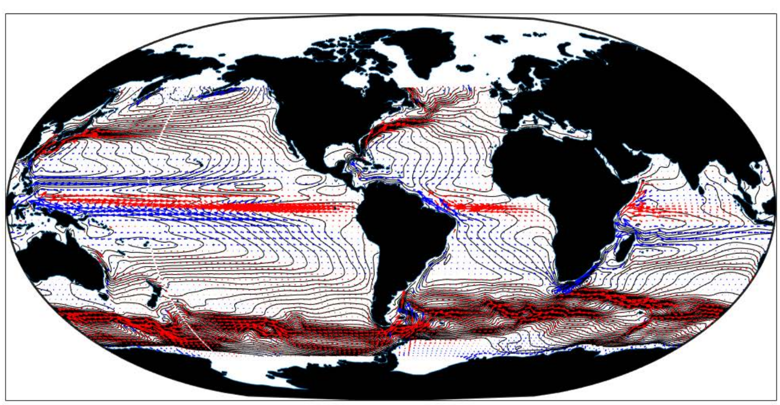

FIG. 21. Same as Fig. 20 except at 105m. The flow is nearly consistent with being fully geostrophic, except on the equator. A strong zonal jet emerges to carry the geostrophic convergence there.

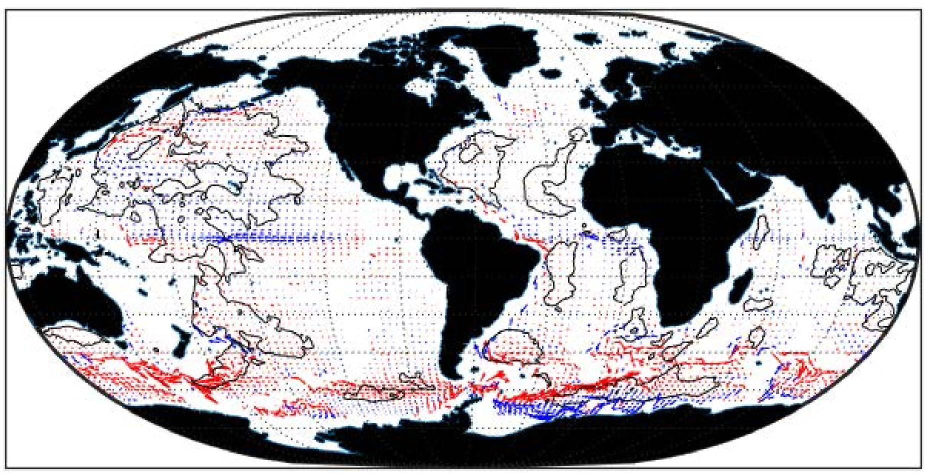

FIG. 22. Twenty-year average horizontal flow at 3600m with the 5000m bottom contour. Largest arrow is 5 cm/s.

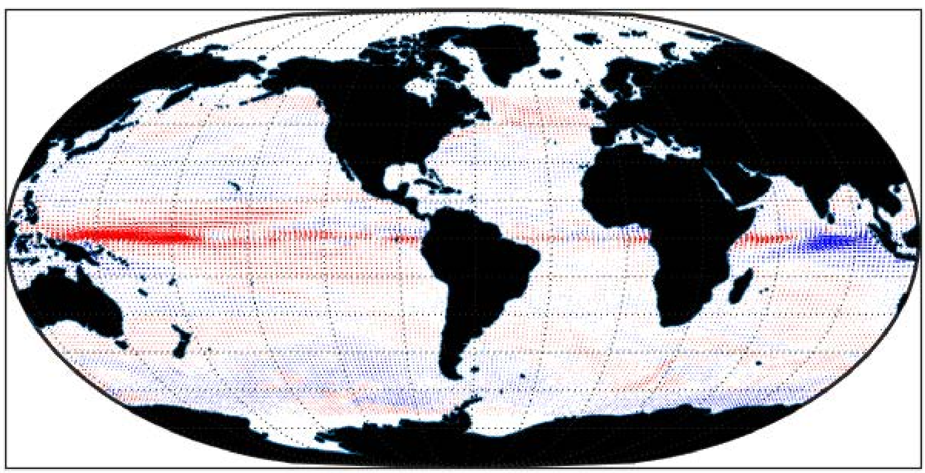

FIG. 23. Anomaly of the 5m horizontal flow in 1994, again with red arrows having an eastward component. Largest arrow is 0.24m/s.

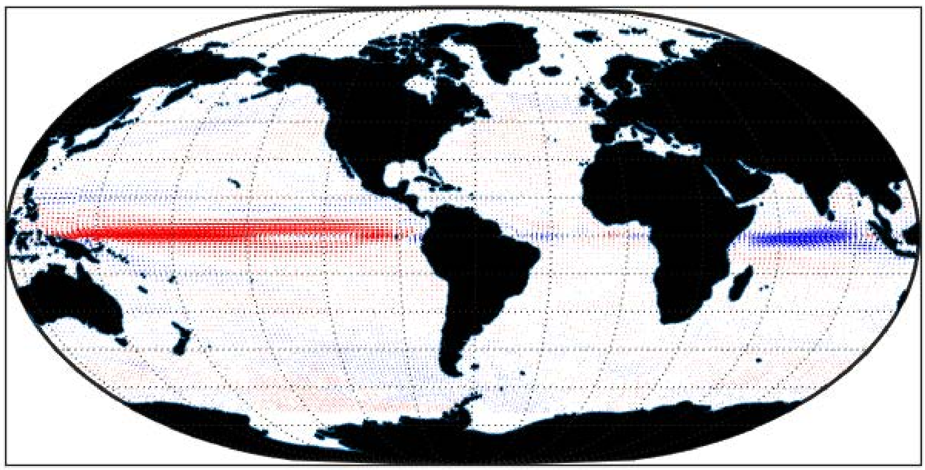

FIG. 24. Same as Fig. 23 except for 1997 with the largest arrow at 0.58 m/s.

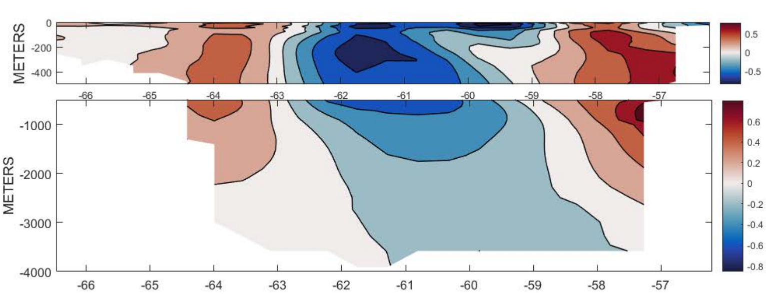

FIG. 25. Anomaly of the zonal flow (cm/s) in the Drake Passage in 1995.

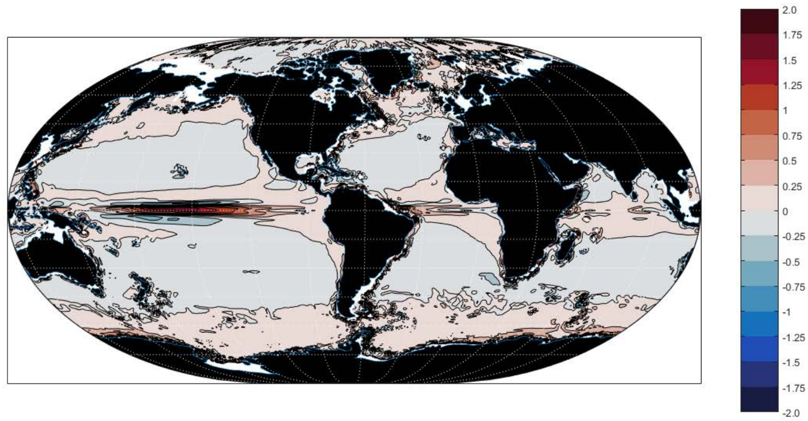

FIG. 26. Twenty-year average vertical velocity ($10^5 w$) (m/s) at 105m depth. This level is an approximate surrogate for the Ekman pumping velocity. The major gyres and equatorial upwelling are readily visible.

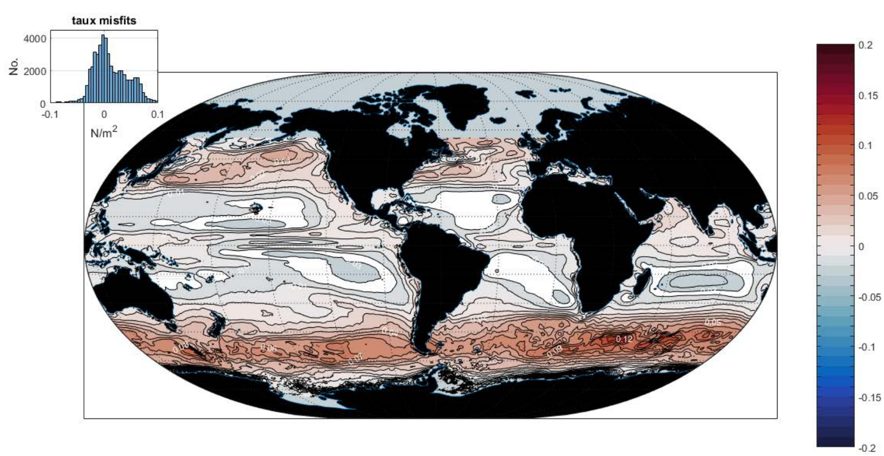

FIG. 27. Adjustments made to the 20-year average zonal windstress, τ_x (N/m^2). This chart can also be interpreted as the average misfit to the ERA-Interim reanalysis. Insert shows the histogram of adjustments, skewed positively.

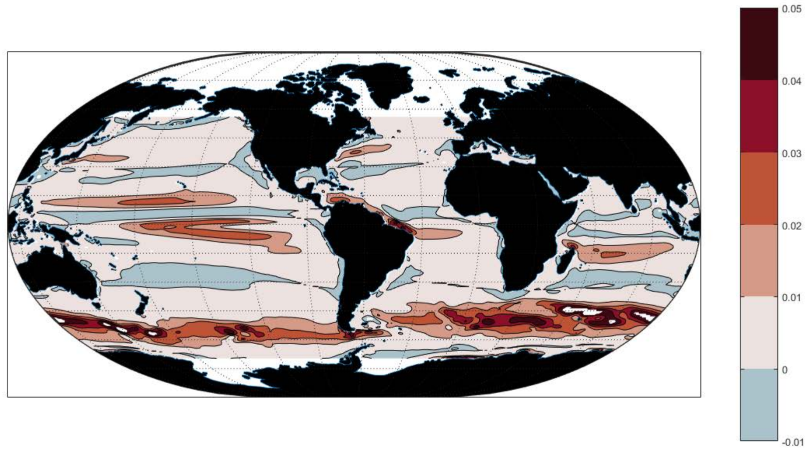

FIG. 28. Rate of working of the mean zonal windstress on the surface circulation (W/m^2). Cf. Wunsch (1998), Zhai et al. (2012), Roquet et al. (2011).

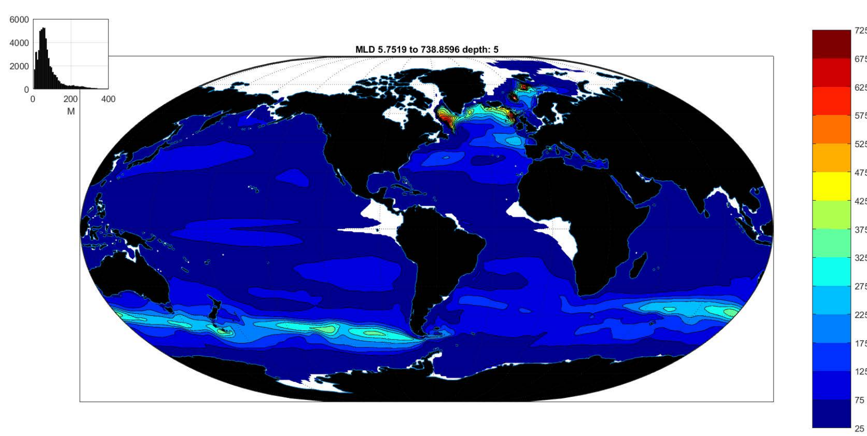

FIG. 29. Twenty-year average mixed-layer depth as defined by Kara et al. (2003). Most of the ocean has values near 100m, with extreme values above 700m in the high latitude North Atlantic Ocean.

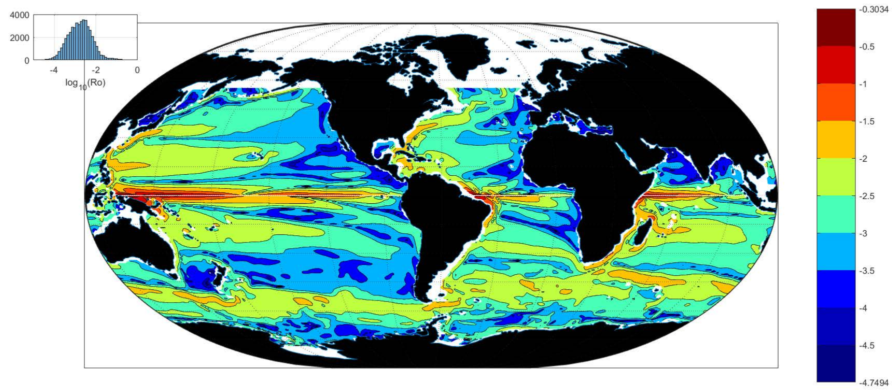

FIG. 30. Logarithm to the base 10 of the estimated Rossby number, based upon a 100km horizontal scale at 410m depth and the 20 year average horizontal speed.

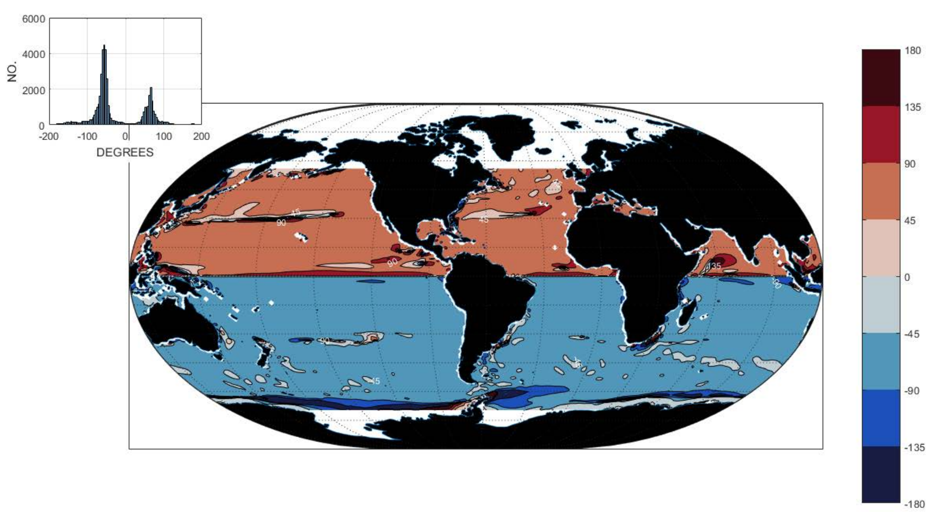

FIG. 31. Angle in degrees between the 20-year average ageostrophic flow at 5m and the 20-year average adjusted windstress. At the sea surface, a perfect Ekman layer would produce $\pm 45^\circ$ with the sign changing across the equator. Inset shows the bimodal histogram of angle values.

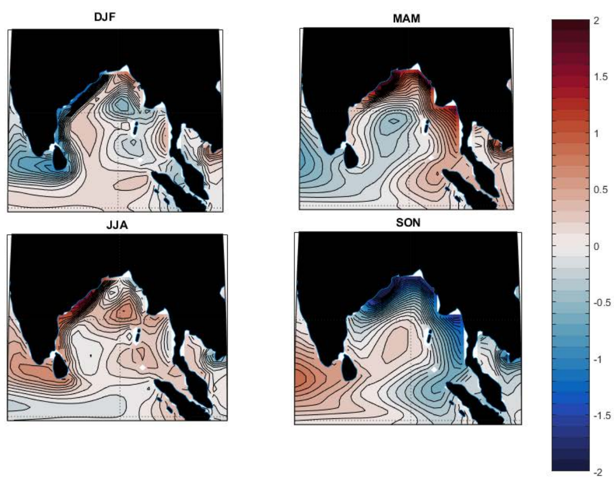

FIG. 32. Twenty-year seasonal averages of salinity anomalies, g/kg, at 5m in the Bay of Bengal.